

# Capability of Helicopter CFD-Simulation Trimmed to Free Flight Condition to Predict Flight Test Data

**Martin Embacher\***, **Manuel Keßler\***, **Markus Dietz\*\***, **Ewald Krämer\***  
Ph.D. Student      Research Associate      R&D Engineer      Professor

\* IAG, Universität Stuttgart, Pfaffenwaldring 21, 70550 Stuttgart, Germany  
\*\* Eurocopter Deutschland GmbH, München, Germany

e-mail: [embacher@iag.uni-stuttgart.de](mailto:embacher@iag.uni-stuttgart.de), [kessler@iag.uni-stuttgart.de](mailto:kessler@iag.uni-stuttgart.de)

## ABSTRACT

This paper presents a comparison between flight test data and simulation results obtained from trimming a computational fluid dynamics model of a complete helicopter to free flight conditions. Trim of rotor controls and helicopter attitude is accomplished by coupling the flow solver with a comprehensive rotor code. Through weak fluid-structure coupling aeroelastic effects at the main rotor are accounted for. The two cases examined are cruise flight and a condition near minimal power consumption. Control and attitude angles, mast moments, blade stresses and power consumption are compared to measured data. Concluding, the usefulness of the free flight trim method for performance prediction is evaluated.

## NOTATION

FLOWer	DLR's structured Finite-Volume flow solver
HOST	Helicopter Overall Simulation Tool
RANS	Reynolds-Averaged Navier-Stokes equations
$\theta_0$	Main rotor collective blade pitch
$\theta_{C,S}$	Main rotor cyclic blade pitch
$\theta_{TR}$	Tail rotor collective blade pitch
$\Psi$	Blade azimuth / yaw attitude positive nose
right	
$\Theta$	Helicopter pitch attitude, positive nose up
$\Phi$	Helicopter roll attitude, positive right
$F_{3D}^n$	CFD loads transferred to HOST at trim n
$F_{2D}^n$	HOST-internal aerodynamic loads at trim n
$F_{HOST}^n$	Loads employed by HOST at trim n
$C_{x,y,z}$	Force coefficients,
$C_{Mx,My,Mz}$	Moment coefficients about hub center,

in the helicopter system of reference:

x	Pointing upward
y	Pointing rearwards
z	Pointing to the right

## INTRODUCTION

Aerodynamic interactions between the helicopter rotor and fuselage (cf. [1]) can take considerable influence on the helicopter performance and trim state. This is due to the drag and download incurred by interference. To a minor degree it also stems from altered rotor inflow at the modified flight attitude, and from additional hub moments demanded from the rotor to counteract the interference loads. At the same time, rotor-fuselage interference itself depends on the trim state.

Computational fluid dynamics (CFD) enables simulation of complete helicopter configurations and inherently captures interference. To determine its effect on the helicopter trim state, coupling the flow solver to a structural dynamics (CSD) and flight mechanics program is necessary. In the standard application, such coupling accounts for the aeroelasticity of the rotor blades and performs the task of rotor trimming by adjustment of collective and cyclic pitch angles. This manipulation of three trim variables commonly is referred to as "wind tunnel trim", as it is geared towards the reproduction of wind tunnel experiments with pre-defined rotor mast orientation. With the rotor held in place by the mounting fixture of the wind tunnel balance, thrust and moments are parameters that are precisely measurable and that are representative of the aerodynamic and dynamic state of the rotor. Hence matching the measured values usually warrants optimal conditions for the aeroelastic part of the simulation task. However, as the wind tunnel trim is based on a fixed orientation of the rotor axis, it has only limited applicability to the study of realistic flight situations; in flight the rotor axis varies as the helicopter assumes an attitude that corresponds to an equilibrium of loads for the entire aircraft. In the case of steady unaccelerated flight, weight and aerodynamic loads arising at the fuselage, the empennage and through engine thrust need to be balanced by the rotor loads in all axes; this requires to raise the number of load objectives accessible through trim from three to six. Accordingly, the formerly three main rotor control inputs are supplemented by two attitude angles and by the tail rotor collective. They thus form a set of six independent, usually coupled, control inputs, and the expanded trim procedure is termed "free flight trim".

Previous work in the direction of free flight trim was presented in [2] and [3], where trimming the mast orientation was included in the coupled isolated rotor simulation to predict vibratory loads for level flight cases of the UH-60A Airloads Program. Fuselage loads were obtained from wind tunnel experiments in this reference. Also in the context of the UH-60A program, and investigating a

steady as well as an unsteady maneuvering flight condition, a tight fluid-structure coupling scheme at the rotor blades was embedded in an inverse flight mechanics simulation in [4]. Again, the isolated rotor was simulated and fuselage aerodynamic loads were obtained from table look-up. Reference [5] includes the fuselage in the CFD model of a tandem helicopter configuration, but in trimming an empirical model for fuselage lift, drag and pitching moment was used. In [6] tabulated fuselage data is used in conjunction with CFD determined interference loads. Steady flow simulations with and without actuator disk provided the load component due to interference. For various flight conditions of an NH-90 like configuration the impact of rotor-fuselage interaction on the trim state was estimated.

The present study considers a free flight trim of a complete EC145 helicopter CFD model, including fluid-structure coupling at the rotor blades. It constitutes a direct continuation of the work in [7], with the focus now placed on the applicability of the method to predict experimental free flight results. Another emphasis is on the dependence of trim state prediction on model features such as engine flow modeling and skid-fuselage interference. Flight test data obtained by Eurocopter is used as experimental reference. Two cases are examined; the first case covers the high speed cruise regime and essentially is identical to the subject of the trim scheme convergence study in [7]. It has been re-computed with an updated model for main and tail rotor and complete blade load transfer to enable a meaningful comparison to flight test data. The second case represents an intermediate flight speed condition near the minimum of the power curve. The discussion of results in comparison to the measurement data is followed by considerations on the usefulness of the free flight trim method for performance prediction.

## NUMERICAL MODELS

For brevity, the following section contains a description of the essential coupling functionality; details on the scheme may be found in the preceding paper [7].

### Flow Solver

The CFD method used is the structured Finite-Volume RANS scheme FLOWer developed by the German aerospace research center DLR. FLOWer solves the three-dimensional, compressible and unsteady Reynolds-Averaged Navier-Stokes equations using a Finite Volume method on block-structured meshes. The equations are formulated in a non-inertial reference system with explicit contributions of centrifugal and Coriolis forces to the momentum and energy equations. Convective fluxes are computed using the JST scheme [8] which uses 2nd order central differences with artificial dissipation for stabilization. For unsteady flow calculations the dual time stepping technique with a second order implicit time integration operator is employed [9]. The integration in pseudo time is carried out using a 5-stage hybrid Runge-Kutta method. Furthermore, FLOWer includes the Arbitrary Lagrangian-Eulerian (ALE) formulation which facilitates the computation of deforming meshes by adding whirl-fluxes. The Geometric Conservation Law (GCL) evaluates the cell volumes of the deformable mesh consistent to the cell face

velocities. This ensures the preservation of uniform flow on deformable grids. The Chimera technology of overlapping grids allows for relative motion of the deformable grids [10]. Chimera connectivity is determined using hole cutting and interpolation.

### Aeromechanics Code

The Eurocopter in-house comprehensive rotorcraft code HOST [11] is mainly used for flight mechanics purposes and enables the study of single helicopter components like isolated rotors as well as complete configurations. HOST trims the rotor based on a blade element formulation with 2D airfoil tables. Airframe component aerodynamics is provided by polars. HOST includes an elastic blade model which considers the blade as a quasi one-dimensional Euler-Bernoulli beam. It allows for deflections in flap and lag direction and elastic torsion along the blade axis. Rigid segments are connected through virtual joints, allowing for geometrical nonlinearities. Possible offsets between the local cross-sectional center of mass, aerodynamic center, tension center and shear center are accounted for, thus coupling bending and torsional degrees of freedom. According to a Rayleigh-Ritz approach, blade deformation is expressed by modal shapes in the radial direction and associated time-dependent general coordinates. The modal basis is obtained by an eigenvalue analysis of the beam in vacuum, resulting in coupled flap and lag mode shapes and decoupled torsion modes.

### Fluid Structure Coupling and Trim

The implementation of free flight trim option is based on the extension of the existing rotor load coupling between the CFD solver and the aeromechanics code (cf [12]) towards a transfer of both rotor and fuselage loads. Figure 1 illustrates the general options for data exchange when coupling a CFD solver and a comprehensive rotor code.

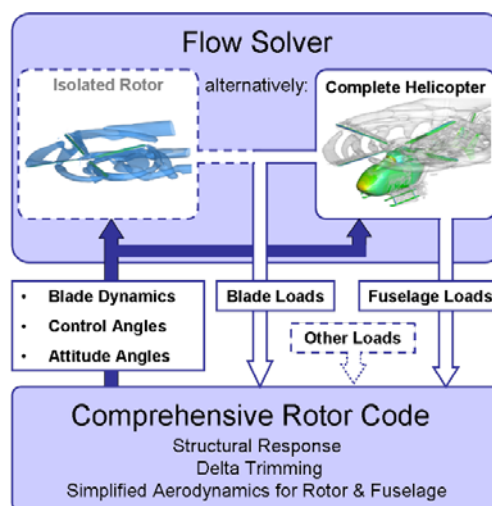


Figure 1: Schematic of data exchange between flow solver and aeromechanics code.

In the case of classical isolated rotor simulations in CFD, only blade loads are forwarded and take corrective influence on the comprehensive code's simplified aerody-

dynamic model. If fuselage aerodynamic data in the form of separately generated polars is made available to the comprehensive code, a simplified variant of free flight trim would be possible with this setup; however, this approach does not take interference effects between the rotor wake and the fuselage into account. Alternatively, when a complete helicopter is modeled in CFD, both blade and fuselage loads including the effects of interference are transferred and enter the trim state prediction. Fluid-structure coupling between FLOWer and HOST is done in a “weak” fashion, i.e. periodic loads are exchanged. Conversely, the set of trim variables calculated by HOST and forwarded to the flow solver equally describes a periodic state. The specific steps of the iterative coupling procedure are as follows:

1. HOST determines an initial trim state based on its internal aerodynamics. This state is termed “trim 0”. FLOWer calculates loads for the blade motion and fuselage attitude provided by HOST.
2. In the subsequent trim iteration, HOST employs the FLOWer load data to correct its internal aerodynamics. Accordingly, load coupling is implemented by setting

$$F_{HOST}^{n+1} = F_{2D}^{n+1} + \left( F_{3D}^n - F_{2D}^n \right). \quad \text{eq. 1}$$

Superscript  $n$  denotes the trim iteration count, and  $F_{3D}^n$  and  $F_{2D}^n$  are the CFD and HOST loads from the previous cycle, respectively. Their difference represents the aerodynamic correction applied. In the current trim iteration  $n+1$ , trim variables are adjusted such that internal aerodynamic loads  $F_{2D}^{n+1}$ , corrected by the term in brackets, yield a load  $F_{HOST}^{n+1}$  that fulfills the trim objective. Adjustments are based on the trim Jacobian established from HOST-internal aerodynamics.

3. FLOWer loads for the trim  $n+1$  are calculated.

Steps 2 and 3 are repeated until convergence of the trim variables. In the trimmed state, CFD loads replace the comprehensive code aerodynamics,  $F_{HOST}^{n+1} = F_{3D}^n$ . The entirety of aerodynamic loads is in balance with the helicopter weight in the temporal mean, and a dynamic equilibrium is established at the rotor blades. By fulfilling the integral load balance in the temporal mean despite the periodic oscillation of main rotor thrust and the short-term variations of fuselage loads, rigid body oscillations of the helicopter as a whole are filtered out. Accordingly, only average values of the fuselage loads are transferred, with the averaging interval extending over at least one and up to five rotor revolutions in the present study.

Blade loads calculated by FLOWer are delivered to HOST in the form of line loads. In addition to transferring sectional lift, drag and pitching moment (as in [7]), also the radial load component is exchanged. Furthermore, the treatment of CFD loads on HOST side has been revised to improve conservativity of the load exchange; previously, the line load attributed to one HOST aerodynamic panel was considered constant over its span and was obtained from interpolating the CFD loads at the panel midpoint. This approach is not strictly load conservative for non-linear load variations and lacks the free moments acting

about the panel midpoint due to load gradients. Although these errors become small at sufficient discretization in HOST, the interpolation was replaced by a strictly conservative method based on integration. The line loads from CFD are integrated over the panel span, and likewise moments acting about the panel collocation point are determined from the CFD load distribution. The relative error between total rotor load in CFD and transferred loads was tested to be less than 0.02% in force at the trimmed state of the cases studied.

A load input termed “other loads” in Figure 1 is used to introduce time averaged hub loads, which are not covered by the CFD model but were obtained from wind tunnel measurements. If the landing gear is not represented in the simulation, additional estimates enter HOST at this point. Since no load coupling at the tail rotor is implemented to date, tail rotor thrust in the CFD simulation was trimmed to the thrust calculated by HOST based on a sensitivity study. The HOST value, ensuring yaw moment balance at the current trim iteration, is considered as objective for the manual setting of tail rotor collective.

### Simulation Setup

The structural model of the main rotor employed during several early trim cycles features 43 beam elements and a modal deformation basis of eight radial eigenforms and five higher harmonics of the rotor period. The upgraded version used for final trim convergence is based on 60 beam elements; hinge characteristics are adapted to improve pitch-lag coupling, and blade motion is resolved with eight harmonics, four flap modes, three lead/lag modes and three torsion modes.

The CFD mesh is composed of 11 Chimera multi-block grid components, which are the fuselage mesh, four main rotor blade meshes, two tail rotor blade meshes and four additional grid structures generating the skid landing gear. Table 1 lists the dimensions of each component. The fuselage mesh serves as a background mesh, i.e. it expands to the far field where characteristic boundary conditions are prescribed. The landing gear is attached to the cabin bottom side using Chimera with overlapping walls. In the overlapping area around the cabin-skid junction, surface patches with coinciding boundaries are defined in the fuselage mesh and the attached cross-tube meshes to enable a correct load evaluation.

Table 1: Dimensions of grid system.

	Blocks	Cells
Main rotor blades	$4 \times 35$	$4 \times 1.750.016$
Fuselage	94	8.487.680
Skids	112	6.936.064
Tail rotor blades	$2 \times 11$	$2 \times 1.382.400$
Total	392	25.188.608

Engine exhaust and air intake are modeled by setting characteristic boundary conditions at the inlet and outlet surface segments. At the outlet, uniform values for total pressure, total temperature and flow direction are specified.

The condition at the inlet requires static pressure to be set. Using the mass flux coupling function of the code, inlet static pressure is adjusted according to

$$\Delta p = \xi p_\infty (\dot{m}_{IN} / \dot{m}_{OUT} - 1), \quad \text{eq. 2}$$

where  $\xi$  is a relaxation parameter, set to  $\xi = 0.10$ , and  $\dot{m}_{IN}$  and  $\dot{m}_{OUT}$  are the integrated mass fluxes. Adjustments take place at every subiteration of the dual time stepping scheme. To date, such automatic adjustment is not implemented for the outlet; therefore, the overall mass flux is controlled by manually setting and re-adjusting the total pressure and temperature at the outlet. Mainly as an effect of blade passage the back pressure at the exhaust is unsteady, which causes the mass flow to fluctuate at an amplitude of approximately 6% to 7% about the mean value. With the mass flux coupling relaxed by  $\xi = 0.10$  the oscillations are reproduced without problems at the inlet. Target values for average mass flow and exhaust temperature are obtained from flight test data and are considered fix, i.e. no correlation with simulated power consumption is considered. For the turbulent kinetic energy free stream values are prescribed at the outlet boundary for lack of information on the actual conditions within the ejector. Further information on the engine boundary conditions can be found in [13], where the model is discussed for a nearly identical case. The thrust associated with the pressure and momentum change between intake and outlet is coupled into the load balance via the load input termed “other loads” in Figure 1.

A physical time step of  $1^\circ$  main rotor azimuth is chosen for all simulations, based on the satisfactory results with this resolution in previous applications of weak coupling to isolated main rotors. To converge in pseudo time 40 inner iterations are used. For the closure of equations the Wilcox  $k-\omega$  turbulence model was selected.

Since the free flight trim procedure requires attitude changes of the helicopter, an unsteady motion of the mesh system is specified to reorient the helicopter within the first 90 time steps of a new trim cycle. This way, the change in inflow direction is the effect of whirl fluxes, which was found to be faster than sole convection of new boundary conditions.

The two simulated flight cases are steady forward flight conditions at 136kts (advance ratio  $\mu = 0.32$ ) and at 70kts ( $\mu = 0.17$ ). An impression of the rotor and fuselage wakes at 136kts can be gained from the  $\lambda_2$  visualization in Figure 2.

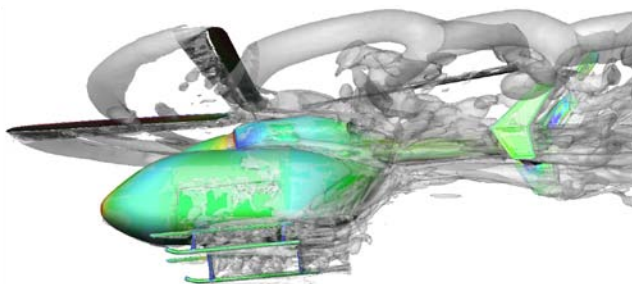


Figure 2: FLOWer simulation of EC145 helicopter,  $\mu=0.32$ .

The 136kts case initially is simulated without skids and engine model, using an estimate for the skid loads and for the related interference loads. This estimate has been obtained by comparing two simulations of the same trim state with and without the skid landing gear. The fuselage yaw, pitch and roll angles in this state were  $\psi = -1.62^\circ$ ,  $\Theta = -0.63^\circ$ ,  $\Phi = -2.26^\circ$ . More details on the interference study can be found in [7]. After trim convergence of the baseline simulation, the Chimera mesh components that generate the landing gear are re-introduced in order to verify the skid load assumption. Finally, a simulation featuring the skids and engine modeling is carried out also for the trim state obtained with the baseline configuration. The setup for the simulations at 70kts employs the skids and the engine model during all trim cycles. For the converged trim state, an additional simulation with prescribed laminar-turbulent transition at the rotor blades is carried out.

## TRIM CONVERGENCE

### General Procedure

Flight test data contains measurements of the fuselage pitch and roll angle, but lacks a precise recording of the yaw angle. Therefore a trim law was chosen that prescribes the measured roll-left attitude of  $\Phi = -2.26^\circ$ , while fuselage pitch angle and the unknown yaw angle are free to develop in the course of trimming. In combination with the main rotor controls  $\theta_0$ ,  $\theta_C$ ,  $\theta_S$  and the tail rotor collective angle  $\theta_{TR}$  six inputs are obtained that allow to trim the helicopter towards the force and moment equilibrium in all three axes. The trim history of the 136kts case is shown in Figure 3, where main rotor control angles are plotted over trim cycle, and in Figure 4 which contains the tail rotor collective and the attitude angles. Control angles are given as offsets from the flight test value. Trim 0 designates the HOST stand-alone solution, while subsequent trim cycles are trim predictions based on CFD load coupling. The entire trim process extends over eleven iterations. This duration is not representative of the convergence rate as several modifications of the HOST model are implemented at trim cycles 5 and 7. The upgrade of the structural model of the rotor at trim 7 is followed by disturbances particularly visible for the main rotor collective angle. As the modifications mainly affect the main rotor controls and elastic blade motion, two trim cycles from trim 10 onwards are carried out by updating only the rotor loads, while the fuselage load correction is kept unchanged. These “sub-iterations” are numbered 10-2 and 10-3. Exclusively converging the trim and aeroelastic state of the rotor saves computational time as the determination of rotor loads by CFD requires simulation times in the order of only one rotor revolution. On the contrary, fuselage loads are highly irregular due to flow separation at the rear cabin closure, and precise mean values can only be obtained by averaging over several rotor revolutions. Therefore, CFD simulation time per trim cycle ranges in between two and four revolutions except for sub-trims. The final trim state, cycle 11, is based on a three-revolution-average of fuselage loads obtained from simulating four revolutions of the state 10-3. Small changes below  $0.01^\circ$  of the trim variables confirm convergence at this point. Therefore no CFD simulation is carried out for state 11, which is signified by the dashed line. Convergence can also be expressed in form of residual

accelerations of the helicopter. Subtracting helicopter weight from the CFD loads of trim state 10-3, the deviation from unaccelerated flight is determined as less than  $0.020\text{m/s}^2$  in translation and  $2.4\text{deg/s}^2$  in rotation.

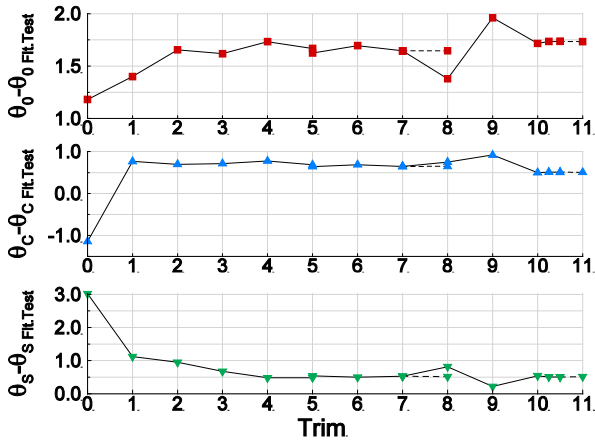


Figure 3: Trim history of main rotor control angles, 136kts.

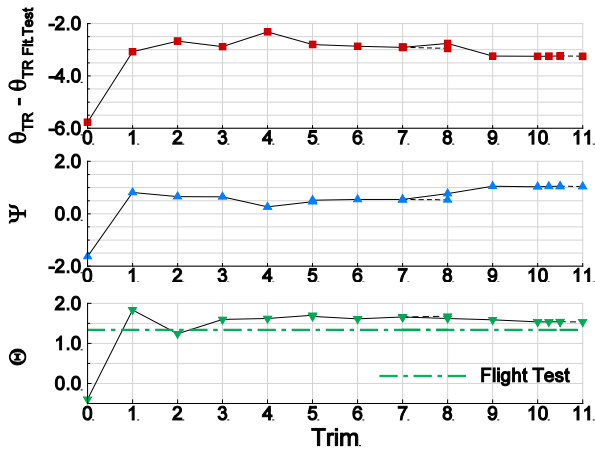


Figure 4: Trim history of tail rotor collective angle, fuselage yaw angle  $\psi$  and pitch attitude  $\Theta$ , 136kts.

The computational effort to reach this state can not directly be recognized from the trim history due to the intermediate HOST modifications. Dashed lines from trim 7 to trim 8 mark a trim state prediction by HOST that indicates convergence of the process before the major upgrade of the rotor model in HOST. This suggests that not more than seven trim iterations are necessary, which are based on a total of 28 rotor revolutions simulated by CFD. Aiming at a less converged state, i.e. permitting control and attitude angle deviations greater than  $0.01^\circ$ , considerably reduces the effort in this case.

The trim evolution of the 70kts case is summarized in Figure 5 and Figure 6. Similar to the 136kts case the upgrade of the HOST model introduces disturbances at trim 5, and convergence of the rotor trim state subsequently is advanced by two sub-iterations 5-2 and 5-3. Trim 6 is simulated in CFD over four rotor revolutions in the standard, fully turbulent boundary layer treatment. Load averaging over the last three revolutions yields the HOST prediction of trim 7. This state is not completely converged, since the yaw angle in particular still develops. Variations in main rotor controls and pitch attitude however are small, and because of limited computational resources the trim process was concluded. In total 26.5 rotor revolutions were

simulated. Residual accelerations derived from the CFD loads for trim state 6 are less than  $0.015\text{m/s}^2$  and  $1.7\text{deg/s}^2$ . Compared to the 136kts case, deviations from the equilibrium state in terms of attitude angles generate less acceleration due to reduced dynamic pressure at the fuselage.

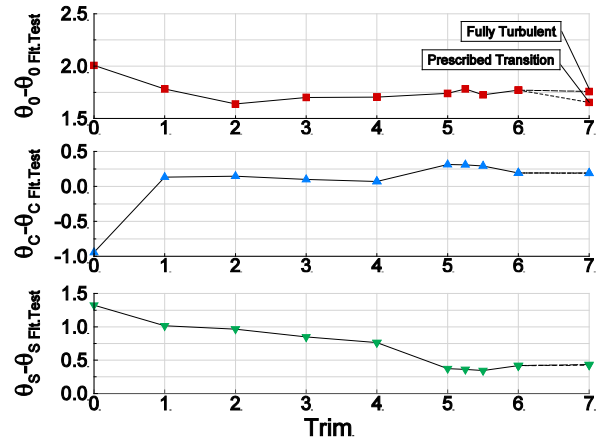


Figure 5: Trim history of main rotor control angles, 70kts.

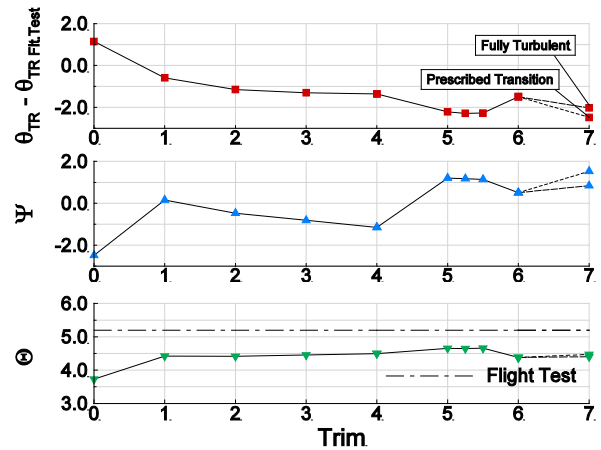


Figure 6: Trim history of tail rotor collective angle, fuselage yaw angle  $\psi$  and pitch attitude  $\Theta$ , 70kts.

## INFLUENCE OF MODELING DETAIL

### 70 kts Case, Prescribed Transition

The second HOST prediction of trim state 7 in Figure 5 and Figure 6 is based on a CFD simulation utilizing prescribed transition at the rotor blades. Restarting the simulation from the fully turbulent solution, one rotor revolution is calculated. The trim change is caused by updated rotor loads only, while the fuselage aerodynamic correction is kept unchanged. Turbulence production is suppressed in a layer stretching over 20% of chord on the upper and 60% of chord on the lower blade surface, independent of radius and blade position. These values are chosen heuristically, inspired by a report [14] on transition locations observed in a full-scale hover experiment. The main purpose of this simulation is to compare the relative reduction of power associated with this laminar flow prescription for the 70kts case and for a regular cruise speed condition. Since power consumption is nearly halved at 70kts, the reduction affects a considerably higher fraction of total power. In [15], an isolated rotor of the same type was simulated with FLOWer at a cruise flight situation similar to the 136kts

case. Prescribing transition at 10% and 60% chord on the upper and lower surfaces, total power was reduced by ca. 4%. This compares to a difference in power consumption of 8.2% between the two states of trim 7 of the 70kts case.

### 136 kts Case, Setup including Skids

Subsequent to trim convergence of the 136kts baseline case, the same trim state 10-3 is simulated with a CFD setup including the landing gear. Load difference of both configurations is obtained after averaging over three rotor revolutions. Skid loads and fuselage load due to interference are summarized in Figure 7 and Figure 8.

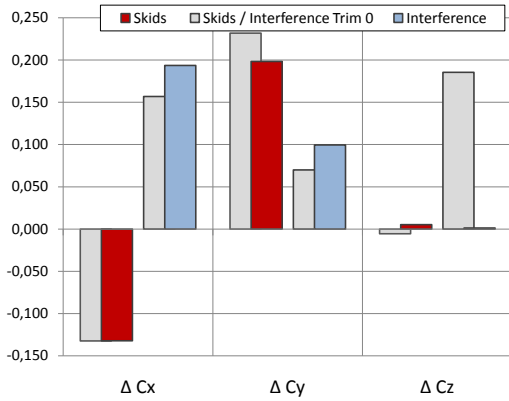


Figure 7: Skid loads and interference effect on fuselage due to inclusion of skids, force coefficients, Trim 10-3.

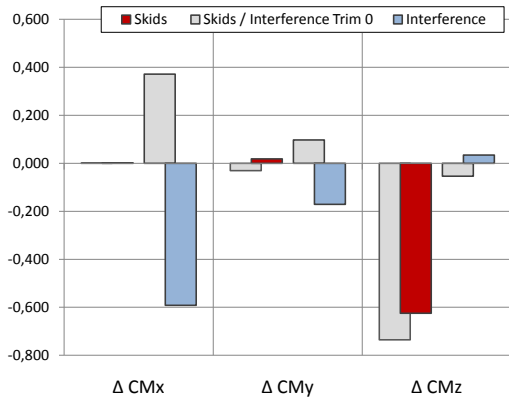


Figure 8: Skid loads and interference effect on fuselage due to inclusion of skids, moment coefficients, Trim 10-3.

The bars colored in light grey represent the skid load estimate used in trimming the baseline case. This estimate was obtained in the same manner from a pair of simulations; the trim state however differs, besides the rotor trim, by  $\Delta\psi = 2.7^\circ$  and  $\Delta\Theta = -2.2^\circ$ , i.e. more yaw to the left and nose-down pitch attitude. Accordingly, the skid loads slightly differ in download and lateral force. More significant is the change in skid drag, which to some extent is caused by differences in flow separation along the rear cross-tube. Most of the difference stems from changed lateral interference force.

A discussion of the validity of the CFD method to predict interference, which is for the most part an effect of altered separation patterns, shall not be attempted here. The results rather are given to approximately illustrate the variability of the interference with changes in trim state, and in order to relate the trim changes caused when updating the interference estimate.

Table 2 lists the trim 11 states for all variants of the 136kts case. Besides the converged baseline case which uses only the symmetric load components ( $\Delta C_X$ ,  $\Delta C_Y$ ,  $\Delta C_{M_Z}$ ) of the skid load estimate, the result of applying all load components of the estimate is given. This can directly be compared with the trim prediction based on the simulation including the skids. Besides yaw attitude, the trim variables are not much affected by the update of the skid loads since the overall symmetric load components change little. Hence, employing the skid load estimate with the trim-sensitive asymmetric components disregarded proves a useful simplification in the present case if the yaw angle is of no particular interest.

Table 2: 136kts case, trim 11 result for different variants.

Trim11	$\theta_0 - \theta_{0FT}$	$\theta_C - \theta_{CFT}$	$\theta_S - \theta_{SFT}$	$\theta_{TR} - \theta$	$\Theta - \Theta_{FT}$	$\psi$
Baseline, symm.	1.73°	0.51°	0.51°	-3.25°	0.20°	1.04°
Baseline, complete	1.71°	0.51°	0.53°	-3.47°	0.21°	0.56°
& Skids	1.68°	0.68°	0.60°	-2.43°	0.22°	0.84°
& Skids, Engine	1.48°	0.74°	0.10°	-3.74°	0.96°	0.63°

### 136 kts Case, Setup including Skids and Engine

To investigate the influence of engine thrust and exhaust-airframe interaction on trim and power consumption, trim 10-3 is also simulated with the engine model activated. The landing gear remains part of the setup. Eight rotor revolutions are simulated in total to allow averaging over five revolutions, which is necessary as the flow becomes substantially more irregular upon activation of the engine model in this case. Subharmonic components cause overall load deviations in the order of  $\Delta C_X > \pm 0.1$ ,  $\Delta C_Y > \pm 0.1$  and  $\Delta C_Z > \pm 0.2$  from the average values  $C_X = -1.1$ ,  $C_Y = 0.9$  and  $C_Z = 0.6$ . Irregular drag variation primarily is introduced at the rear cabin closure, while lateral disturbance originates to a great part at the other cabin parts and the engine fairing. It seems that flow spillage sideways off the engine intakes, which changes when the engine mass flow varies in response to unsteady conditions at the outlet, plays a role here. The stabilizer and vertical control surfaces occasionally generate short load peaks.

Load changes from engine activation are determined by subtracting the average loads from three revolutions of the trim 10-3 simulation with just skids. Results are given in Figure 9 and Figure 10. The direct load difference not caused by interference at inlet and outlet, which is taken here as the momentum change plus the pressure force variation caused by activating the engine model, reduces total drag by 14%. Approximately half of the propulsive effect is cancelled by interference drag. Download on the stabilizer and lateral force on the endplates generate significant pitch and yaw moments. Both drag reduction and nose-up moment cause the decrease in collective pitch of  $\Delta\theta_0 = -0.20^\circ$  and the increase in fuselage pitch angle of  $\Delta\Theta = 0.74^\circ$  shown in Table 2. The lowering of  $\theta_S$  is an effect of the pitch attitude change.

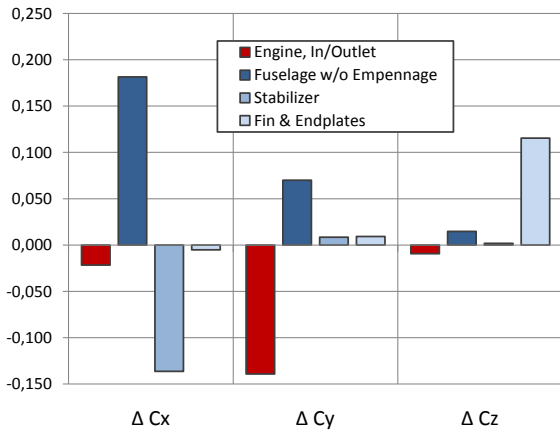


Figure 9: Load changes from activated engine model, force coefficients.

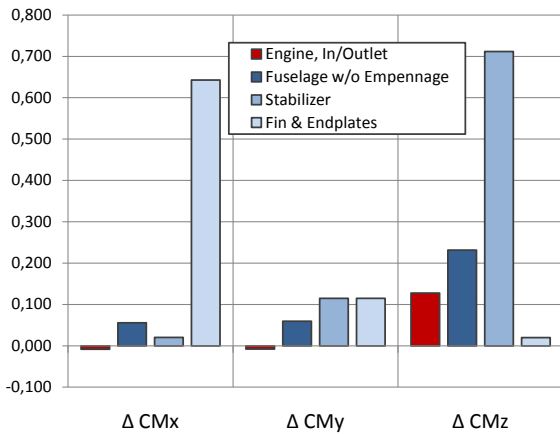


Figure 10: Load changes from activated engine model, moment coefficients.

The interference effect of the exhaust plume on the rotor inflow is remarkably small. Local modifications in sectional lift are less than 1.8% of average sectional lift. Total thrust change through engine effects is less than 0.01%, and rotor overturning moment changes by  $\Delta C_{M_z} = 0.13$ . The alteration in rotor roll moment is negligible, and torque is reduced by 0.11%. Note that all changes are recorded with exactly the same blade motion, i.e. before re-trimming. The lift changes are entirely due to the displacement effect of the exhaust plume, there is no direct interference of the low-density exhaust gas with the rotor.

### COMPARISON TO FLIGHT TEST DATA

In addition to the rotor control and attitude angles, measurements of mast bending moments, stabilizer root bending moment, pitch link load, blade stresses, engine shaft torque and tail rotor transmission torque are available flight testing for both cases. Unless noted otherwise, flight test data of the 136kts case is compared to simulation results of the baseline configuration in trim 10-3, and for the 70kts case simulation data corresponds to trim 6.

Bending stress sensors attached to the root of each stabilizer wing respond to both stabilizer download and endplate lateral force as the endplate aerodynamic center is above the sensor. Therefore, these two sources of bending moment are distinguished in Figure 11 and Figure 12. As a

result of this combination effect, mismatches in either lateral or vertical load can not be detected separately. A comparison with the mast bending moment given in the adjacent diagrams however suggests, that an important part of the discrepancy in stabilizer bending moment stems from a difference in vertical loading. In the 136kts case as well as in the 70kts case, the simulation predicts a higher nose-down bending moment exerted by the rotor on the fuselage, which likely is required to compensate the nose-up pitching moment from the download surplus at the stabilizer.

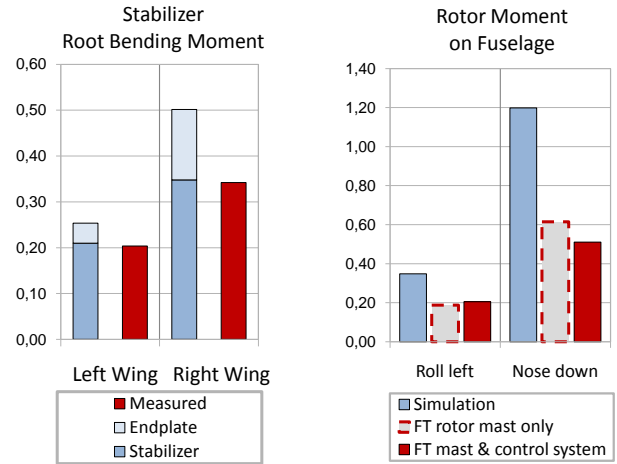


Figure 11: 136kts – Left: Downward bending moments at root of each stabilizer wing. Right: Mean rotor moments.

Left-right comparison of the stabilizer bending moments turns out similar in both cases; both measurement and simulation generate less stress in the left sensor, which probably is due to the reversed-flow region and reduced downwash of the main rotor that affects both the left endplate and left stabilizer wing. Generally, the canted endplate produces lift towards the right which bends the left wing upward, while flow deflection by tail rotor thrust reduces the endplate load to some extent.

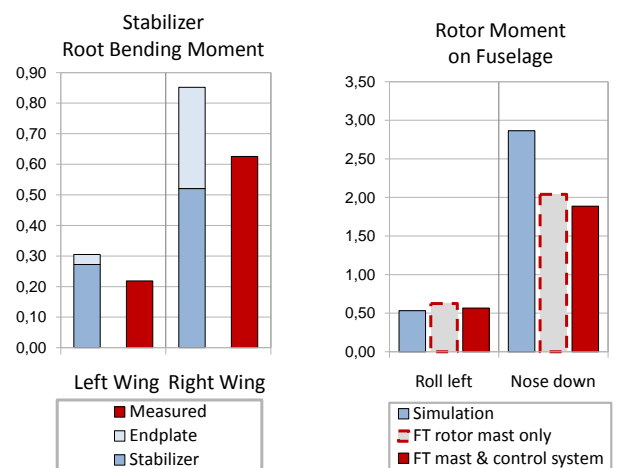


Figure 12: 70kts – Left: Downward bending moments at root of each stabilizer wing. Right: Mean rotor moments.

The treatment of mast bending moment takes the second load path via the rotor control links into account. Mast bending measurements are obtained from strain gauges within the rotor shaft, hence moments generated by the pitch link

loads have to be added to obtain the overall moment exerted by the rotor on the fuselage. Moment transmitted by the pitch link loads generally is nose-up in both cases, which is due to their attachment on the trailing edge side and blade lag in the forward position. Roll moment of the rotor is reproduced well in the 70kts case. Since roll attitude is constant, hub moment generated by weight can be disregarded and the additional roll-left moment in the 136kts simulation is required to compensate an aerodynamic load difference at the fuselage. This load may stem from insufficient nose-right attitude.

Figure 13 compares simulated and measured bending moments in the blade neck for the 136kts case. Mean values have been removed since strain gauge calibration took place at an unknown blade deflection at rest. The 2/rev component of flatwise bending (normal to the local blade chord), which is mainly generated by the 2<sup>nd</sup> flap mode, is well reproduced. For the blade positions between  $\psi = 160^\circ$  and  $\psi = 260^\circ$  the simulated downward bending is higher, while around  $\psi = 0^\circ$  the upward bending moment slightly exceeds the measured values. This corresponds well with the higher nose-down and roll-left mast moment. Edgewise bending mainly is 1/rev periodic, with higher amplitude in the simulation. Assuming that differences in flatwise bending connect to the 1<sup>st</sup> flap mode, part of the deviation in edgewise moment may be explained by additional lead/lag motion induced by the Coriolis effect.

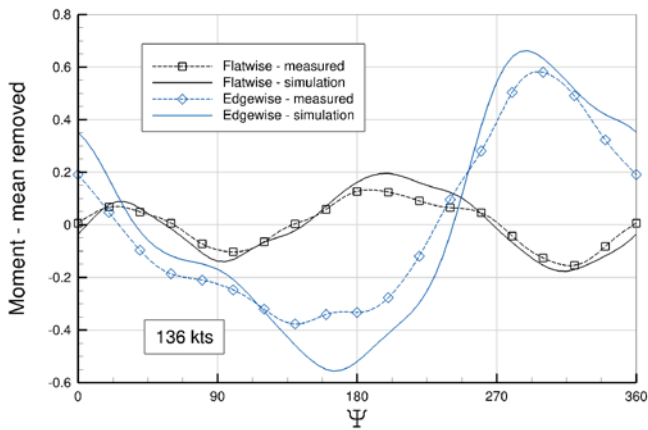


Figure 13: Bending moments in the blade neck,  $r/R=0.095$ , 136kts case. (Positive for downward / forward bending)

Torsional blade stress is recorded at approximately one third of blade span. Figure 14 shows that torsional stress at this location corresponds well with tension load in the pitch link, which is attached at the trailing edge side. The simulation predicts the trend in the first three quadrants but significantly deviates in the last quadrant. Load fluctuations at ca. 10/rev occur in the simulation. High lift in combination with blade lead causes the peak in torsion and pitch link load around  $\psi = 330^\circ$  in the simulation.

For the 70kts case, flatwise bending stress in Figure 15 is well reproduced apart from rear blade positions; in this region higher upward bending is simulated, which is in accordance with the increased nose-down mast moment. Similarly, edgewise bending agrees with the measurement except around  $\psi = 0^\circ$ . The wakes of rotor hub and cap possibly have an influence at the nose-up attitude of the 70kts case, whereas simulation results indicate no interference of exhaust gas with the rotor. Simulated torsion and pitch link loads show some features of the measured data but vary in the 1/rev component, see Figure 16.

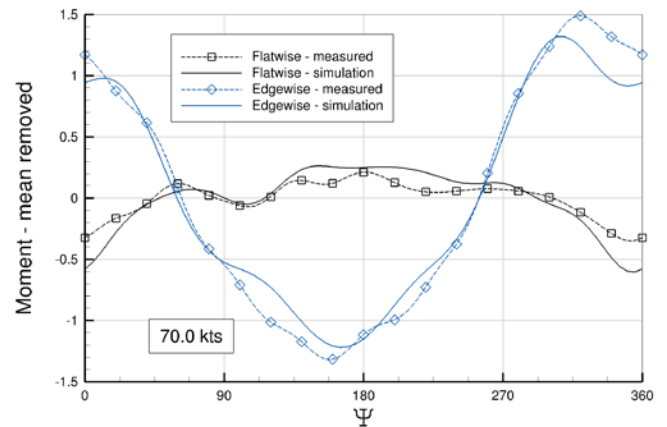


Figure 15: Bending moments in the blade neck,  $r/R=0.095$ , 70kts case. (Positive for downward / forward bending)

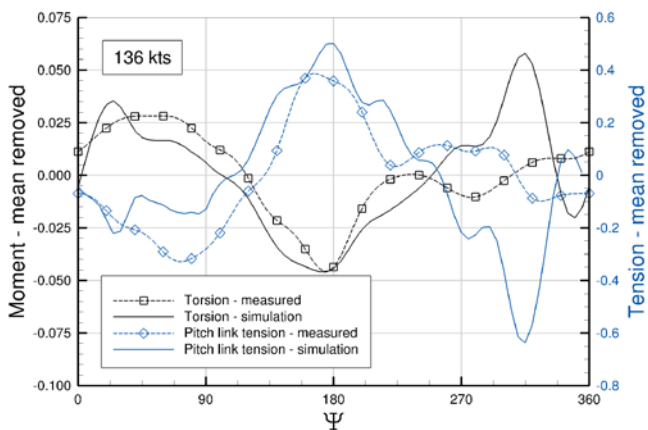


Figure 14: Pitch link load and torsion moment at  $r/R=0.30$ , 136kts case. (Positive for tension / nose-up twist)

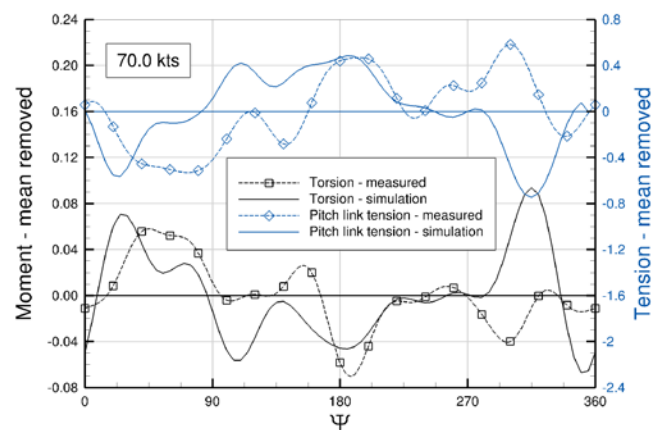


Figure 16: Pitch link load and torsion moment at  $r/R=0.30$ , 70kts case. (Positive for tension / nose-up twist.)

Results for main rotor and tail rotor power consumption for both flight speeds and the different configurations are summarized in Figure 17. The data is given as a percentage of the flight test values. Actual main rotor power is reconstructed from the measurement of engine shaft torque by estimates for gear box and auxiliary device losses. HOST results are from stand-alone calculations, i.e. without FLOWer coupling, but are based on airfoil tables considering laminar flow.

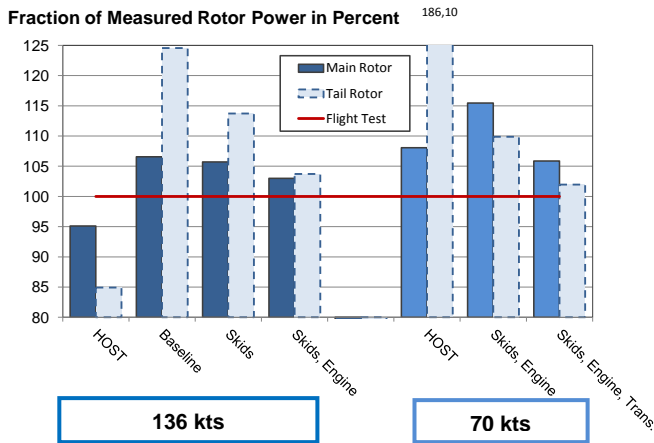


Figure 17: Power consumption in comparison to flight test.

For the baseline configuration, 106.5% of actual power is required in the converged trim state 10-3. The update to trim 11 based on the simulation including skids mainly improves the prediction for tail rotor power, which is due to considering lateral skid interference loads. Evaluating the simulation of trim state 10-3 with both skids and engine effects modeled, the trim update predicts main and tail rotor power consumption within less than 4% from the flight test values. The various effects of engine modeling on performance prediction are discussed in the next section.

For the 70kts case the simulation includes skids and engine external flow; in the nearly converged trim 6 power consumption is overestimated by 15.5% for the main rotor. One subsequent trim update based on a simulation of trim state 6 with prescribed transition reduces main rotor power to 106% of the actual value.

The additional 4% of power predicted for the 136kts case may be explained by the fully turbulent treatment of this case; however, considerable difference in fuselage drag due to the lack of antennas, window sills etc. in the CFD model as well as the artificial viscosity applied still is a source of errors, although they partly might compensate each other. Flow separation from the cabin rear is a general problem. Due to reduced dynamic pressure at the fuselage, these factors are less influential in the 70kts case; nevertheless, the underestimation of nose-up attitude in combination with higher nose-down mast moment indicates that higher drag prevails in the simulation.

Differences in control angles are difficult to judge as it is suspected that there are still deficiencies in modeling torsional coupling effects at the rotor blades. The increased cyclic angle  $\theta_C$  in both cases corresponds to the additional nose-down mast moment. A test for the 136kts case yields nearly the same value as in the flight test when the rotor is

trimmed towards the measured mast moment. Underestimation of tail rotor collective partially is due to suppressed see-saw motion in the CFD model.

## REVIEW OF FREE FLIGHT TRIM w.r.t PERFORMANCE PREDICTION

Helicopter performance can be analyzed by splitting up total power consumption of the main rotor into power absorbed by overcoming the fuselage drag, and into the fraction of power expended at the rotor in the generation of the vertical lifting force component (cf. [16]). This approach differentiates shaft power by losses due to the propulsive and the lifting tasks of the rotor. The latter part of power expenditure is attributed in energy methods to the induced and profile drag that are allotted to the vertical lifting force. In the present treatment, it also encompasses the power losses from hub drag. The power share dissipated by the “parasite” drag of the fuselage and tail rotor can be calculated by multiplying the horizontal rotor propulsion force with flight speed. The division of propulsive power between main and tail rotor depending on tail rotor axis inclination is considered this way, but tail rotor performance is not analyzed further here. Subtracting parasite drag related power from total main rotor power, the power used at the rotor for (vertical) lift generation can be estimated. Division by flight speed converts the lifting power into an “equivalent” drag force  $D$ , which can be related to vertical lift  $L$  to form an “equivalent” lift-to-drag ratio  $L/D$  of the rotor. As this lift-to-drag ratio is obtained after factoring out the losses inferred by the rotor’s propulsive work, which depends on the fuselage design, it is a suitable parameter to evaluate rotor efficiency.

A performance analysis of this kind is used in the following to estimate the usefulness of the free flight trim method for performance prediction. The analysis is carried out for the 136kts case. Considering the equilibrium state of trim 10-3 as the reference solution, changes in the various power shares are monitored while disturbing the equilibrium state by longitudinal force perturbations  $\Delta C_Y$  and pitching moment perturbations  $\Delta C_{M_Z}$ . The perturbations are additional loads applied at the center of gravity and can be understood as the load difference to a solution obtained from an alternative helicopter load prediction method. For instance, if the alternative method does not comprise rotor-fuselage interference effects, the perturbations are considered as the load difference invoked by the omission of interference. They equally can be understood as errors in the interference load prediction, or to some extent also as errors in overall load prediction in comparison with the real loads in the flight test. The perturbed state is the result that would be obtained with the alternative load prediction method.

All perturbations are applied to the HOST model while the aerodynamic correction from CFD is retained or partially updated. HOST further operates in the free flight trim mode and changes in helicopter pitch and yaw attitude occur upon perturbation. For the longitudinal load perturbations of  $\Delta C_Y = \pm 0.1$ , the trim changes predicted by HOST would be reasonably accurate without updating the aerodynamic correction terms. Nevertheless, the trim calculation is carried out employing CFD coupling to improve

accuracy. In case of the pitching moment perturbations of  $\Delta C_{MZ} = \pm 1.0$ , the Pitt & Peters inflow model used in HOST is not capable to predict the power changes, and the use of CFD coupling is necessary. As with the procedure of trim “sub-iterations” described above and used to converge the rotor state after remodeling the structural rotor model, the update of aerodynamic loads only encompasses the rotor loads. Fuselage load correction is kept unchanged, i.e. the correction term used in determining the trim 10-3 is retained. This way, fuselage load changes occur according to the gradients of the HOST internal model, which does not derogate the validity of the study as the perturbations also can be understood as deviations from linear fuselage aerodynamics. Two re-trims are carried out following the initial trim prediction with the perturbation applied. CFD simulation time for the first retrim is one half revolution, including one quarter revolution for the helicopter attitude adjustment. The second retrim is based on the CFD simulation of one complete revolution and leads to a state sufficiently converged for power analysis. Hence, four new trim states were calculated with each state converged by two cycles of rotor load coupling.

Results are summarized in Table 3 for the longitudinal force perturbations  $\Delta C_Y = \pm 0.1$  and in Table 4 for the pitching moment perturbations  $\Delta C_{MZ} = \pm 1.0$ . State variations are described in terms of changes in pitch attitude  $\Delta\Theta$ , in pitch moment  $\Delta C_{MZ}$  exerted by the rotor on the fuselage, in rotor vertical lift, in rotor horizontal force (positive to the rear), in rotor lift-to-drag ratio  $\Delta L/D$ , and in terms of power changes  $\Delta P$  attributed to different components. These power changes are given as percentages of the CFD determined power for trim 10-3. The power change attributed directly to the perturbation is equal to the perturbation force times the flight speed, and does not occur for the moment perturbation. Fuselage drag modifications in consequence of attitude variation are likewise converted into power changes. The fuselage lift change is related to the lift of the perturbed state and multiplied by the rotor power share used for lift generation. The influence of altered rotor efficiency on power consumption is measured by a power change computed from the  $L/D$  variation; this value is calculated by multiplying the relative change of  $L/D$  with the lift-associated rotor power. The direct and three indirect power changes sum up to the total change in shaft power.

Table 3: Trim state change upon longitudinal force perturbation at the center of gravity.

Drag Perturbation $\Delta C_Y$		0.1	-0.1
$\Delta\Theta$ Pitch Attitude	(deg)	-0.373	0.375
$\Delta C_{MZ}$ Rotor Moment	(-)	-0.035	0.039
$\Delta$ Rotor Lift	(-)	0.057	-0.059
$\Delta$ Rotor horizontal force	(-)	-0.106	0.106
$\Delta L/D$ Rotor	(%)	-0.589	0.357
$\Delta P$ Perturbation (direct)	(%)	3.036	-3.035
$\Delta P$ Fuselage Drag	(%)	0.188	-0.187
$\Delta P$ Fuselage Lift	(%)	0.302	-0.310
$\Delta P$ Rotor, $L/D$	(%)	0.416	-0.250
$\Delta P$ Total	(%)	3.942	-3.781

In case of  $\Delta C_Y = +0.1$ , which can be considered as additional drag as long as pitch attitude changes are small, the rotor counters the load increment by a horizontal force of -0.106. This increase in propulsive force is slightly larger than the perturbation itself in order to overcome higher parasite drag encountered in the perturbed trim state. This reflects in the increase of fuselage related power. Likewise, the greater download on the fuselage after nose-down pitching requires more rotor lift and lifting power. Forward-tilting of the rotor tip plane for drag compensation increases inflow and thus reduces the lift-to-drag ratio, resulting in additional power demand. The results for  $\Delta C_Y = -0.1$  indicate an almost linear variation with  $\Delta C_Y$  for all parameters besides the lift-to-drag ratio and the related power change.

For the moment perturbations  $\Delta C_{MZ} = \pm 1.0$ , the pitch attitude change and related power variations are similar in magnitude to the case of a drag perturbation with  $\Delta C_Y = \pm 0.1$ , total power changes however are considerably less as the perturbation generates the power change indirectly. No clear trend for the lift-to-drag ratio is found for the present case, rearward tilt of the rotor shaft in combination with a small increase in propulsive force and the opposite condition both reduce rotor efficiency. The change in pitching moment exerted by the rotor on the fuselage does not counter the entire perturbation since the stabilizer contributes a part of the compensation.

Analyzing the influence of the load changes through engine model activation given in Figure 9 and Figure 10, the power shares can be attributed as follows: Engine thrust by itself, without considering interference effects between the exhaust plume and the fuselage, directly and indirectly diminishes power consumption by 5.2%. Drag changes by interference increase power demand by 3.3%. Leaving aside the question of accuracy of the CFD result for the interference loading on the stabilizer, a change in this order of magnitude causes pitch moments leading to a power reduction of 0.8%.

Table 4: Trim state change upon pitching moment perturbation.

Moment Perturbation $\Delta C_{MY}$		1.0	-1.0
$\Delta\Theta$ Pitch Attitude	(deg)	0.514	-0.514
$\Delta C_{MZ}$ Rotor Moment	(-)	-0.695	0.696
$\Delta$ Rotor horizontal force	(-)	-0.080	0.080
$\Delta$ Rotor Drag	(-)	0.010	-0.010
$\Delta L/D$ Rotor	(%)	-0.183	-0.274
$\Delta P$ Perturbation (direct)	(%)	-	-
$\Delta P$ Fuselage Drag	(%)	-0.292	0.305
$\Delta P$ Fuselage Lift	(%)	-0.426	0.423
$\Delta P$ Rotor, $L/D$	(%)	0.129	0.193
$\Delta P$ Total	(%)	-0.589	0.921

The accuracy gain in performance prediction obtained from free flight trimming stems from the difference in rotor efficiency and in fuselage lift and drag caused by considering attitude variations. These are the indirect  $\Delta P$  components in Table 3 and Table 4 besides the direct  $\Delta P$  attributed to the perturbation, provided fuselage lift and drag variations really follow the gradients the study is based on. In the present case the gradients are those of the HOST model, obtained from wind tunnel experiments of the isolated fuselage. In this “linear” case, the direct power change listed for the perturbation is not a distinct effect of wind tunnel trimming. It can be considered entirely as the result of a defect in the load prediction method, that upon correction evidently is accounted for as the product of the drag change and flight speed. Comparing free flight trim and wind tunnel trim, the perturbations can be considered as the residual non-equilibrium loads present after the wind tunnel trim. The perturbation corresponds to attaching a balance to the free flying model and discharging the loads that arise while prescribing its attitude. In the “non-linear” case, where fuselage drag and lift do not develop according to the estimated gradients, the deviation from the estimated load change can be counted as part of the perturbation. The defect of a load prediction method would be augmented by the defect’s dependence on trim state. As an example, missing rotor-fuselage interference effects may be considered as a defect in load prediction, whereby downwash on the stabilizer depends on attitude and rotor trim. For these “non-linear” effects the benefit from free flight trim can not be quantified with general validity.

For the present flight case and helicopter, employing the gradients of the isolated fuselage and re-trimming the rotor with CFD coupling, the following statements on accuracy gains can be made for the longitudinal trim:

- When resolving a drag imbalance from wind tunnel trim, and/or when employing an improved drag prediction method, the directly calculated power change is augmented by free flight trimming by approximately 27% through the indirect effects of attitude and rotor efficiency change. An increase in fuselage drag (without hub) of 10%, which corresponds to the perturbation  $\Delta C_Y = +0.1$ , directly generates a shaft power increase of ca. 3.0%, while power consumption is raised indirectly by 0.8%. Pitch attitude modifications of  $1^\circ$  correspond to indirect power changes of ca. 2.2% when they are the result of restored balance or improved prediction of drag.
- When resolving a moment imbalance from wind tunnel trim, and/or when employing an improved fuselage pitching moment prediction, the resulting attitude and rotor efficiency variation represented in free flight trim cause approximately 1.5% change in total shaft power per  $1^\circ$  pitch attitude change. With the rotor model used about one third of such a moment change is compensated by the stabilizing moment of the fuselage/empennage, the remainder by rotor moment with a cyclic control input of  $\Delta\theta_c=0.4^\circ$ .

Lateral trim perturbations also take an indirect influence on power consumption, for instance when they translate into drag changes of the fuselage in the course of re-trimming the yaw angle, but were not investigated yet. For lower flight speeds it may be expected that, since induced power of the rotor takes a greater fraction of total power, the rotor L/D change while trimming out load perturbations will gain significance, while the impact of deficiencies in fuselage load prediction reduces.

## ACKNOWLEDGMENTS

The authors would like to acknowledge the support of the German ministry of Economy and Labor (BMWA), providing access to high performance computing in the framework of the HELISIM account. Thanks are extended to employees of Eurocopter for their help with judging the experimental data.

## REFERENCES

- [1] Sheridan, P. and Smith, R., “Interactional Aerodynamics – A New Challenge to Helicopter Technology”, Presented at the 35<sup>th</sup> Annual National Forum of the American Helicopter Society, May, 1979.
- [2] Datta, A., Sitaraman, J., Chopra, I. and Baeder, J.D., “CFD/CSD Prediction of Rotor Vibratory Loads in High-Speed Flight”, Journal of Aircraft, Vol. 43, No. 6, November-December 2006, pp. 1698-1709.
- [3] Datta, A. and Chopra, I., “Prediction of the UH-60A Main Rotor Structural Loads Using Computational Fluid Dynamics/Comprehensive Analysis Coupling”, presented at the 32<sup>nd</sup> European Rotorcraft Forum, Maastricht, The Netherlands, September 12-14, 2006.
- [4] Rajmohan, N., Manivannan, V., Sankar, L., Costello, M. and Bauchau, O., “Development of a Methodology for Coupling Rotorcraft Aeromechanics and Vehicle Dynamics to study Helicopters in Maneuvering Flight”, presented at the American Helicopter Society 65<sup>th</sup> Annual Forum, Grapevine, Texas, May 27-29, 2009.
- [5] Bhagwat, M., Dimanling, A., Saberi, H., Meadowcroft, E., Panda, B. and Strawn, R., “CFD/CSD Coupled Trim Solution for the Dual-Rotor CH-47 Helicopter Including Fuselage Modeling”, Presented at the American Helicopter Society Specialist’s Conference on Aeromechanics, San Francisco, CA, January 23-25, 2008.
- [6] Borie, S., Mosca, J., Sudre, L., Benoit, C. and Péron, S., “Influence of rotor wakes on helicopter aerodynamic behaviour”, Proceedings of the 35<sup>th</sup> European Rotorcraft Forum, Hamburg, Germany, September 22-25, 2009.
- [7] Embacher, M., Keßler, M., Dietz, M. and Krämer, E., „Coupled CFD-Simulation of a Helicopter in Free Flight Trim“, Proceedings of the American Helicopter Society 66<sup>th</sup> Annual Forum, Phoenix, AZ, May 11-13, 2010.
- [8] Jameson, A., Schmidt, W. and Turkel, E.: “Numerical Solutions of the Euler Equations by Finite Volume Methods Using Runge-Kutta Time-Stepping Schemes”, AIAA-Paper 81-1259, 1981.

- [9] Jameson, A.: "Time Dependent Calculation Using Multigrid, With Applications to Unsteady Flows Past Airfoils and Wings", AIAA-Paper 91-1596, 1991.
- [10] Schwarz, Th.: "The Overlapping Grid Technique for the Time-Accurate Simulation of Rotorcraft Flows", Proceedings of the 31st European Rotorcraft Forum, Florence, Italy, September 2005.
- [11] Benoit, B., Dequin, A-M., Kampa, K., Grünhagen, W. v., Basset, P-M., Gimonet, B.: "HOST: A General Helicopter Simulation Tool for Germany and France", American Helicopter Society, 56th Annual Forum, Virginia Beach, Virginia, May 2000.
- [12] Dietz, M., Krämer, E., Wagner, S. and Altmikus, A., "Active Rotor Performance Investigations Using CFD/CSD Weak Coupling", Proceedings of the 34th European Rotorcraft Forum, Kazan, Russia, September 11-13, 2008.
- [13] Le Chuiton, F., "Quasi-Steady Simulation of a Complete EC-145 Helicopter: Fuselage + Main/Tail Actuator Disks + Engines", Proceedings of the 31<sup>st</sup> European Rotorcraft Forum, Florence, Italy, September 12-15, 2005.
- [14] Rohardt, C. H., "Flow Visualization on a Helicopter Rotor in Hover using Acenaphten", Proceedings of the 13<sup>th</sup> European Rotorcraft Forum, Arles, France, September 8-11, 1987.
- [15] Dietz, M., and Dieterich, O., "Towards increased industrial application of rotor aeroelastic CFD", Proceedings of the 35<sup>th</sup> European Rotorcraft Forum, Hamburg, Germany, September 2009.
- [16] Gessow, A., and Myers, G. C. Jr., "Aerodynamics of the Helicopter", College Park Press, Republished 1999.